Volume 13
Number 36
28 September 2025
Pages 18525–19066

Journal of Materials Chemistry C

Materials for optical, magnetic and electronic devices

rsc.li/materials-c

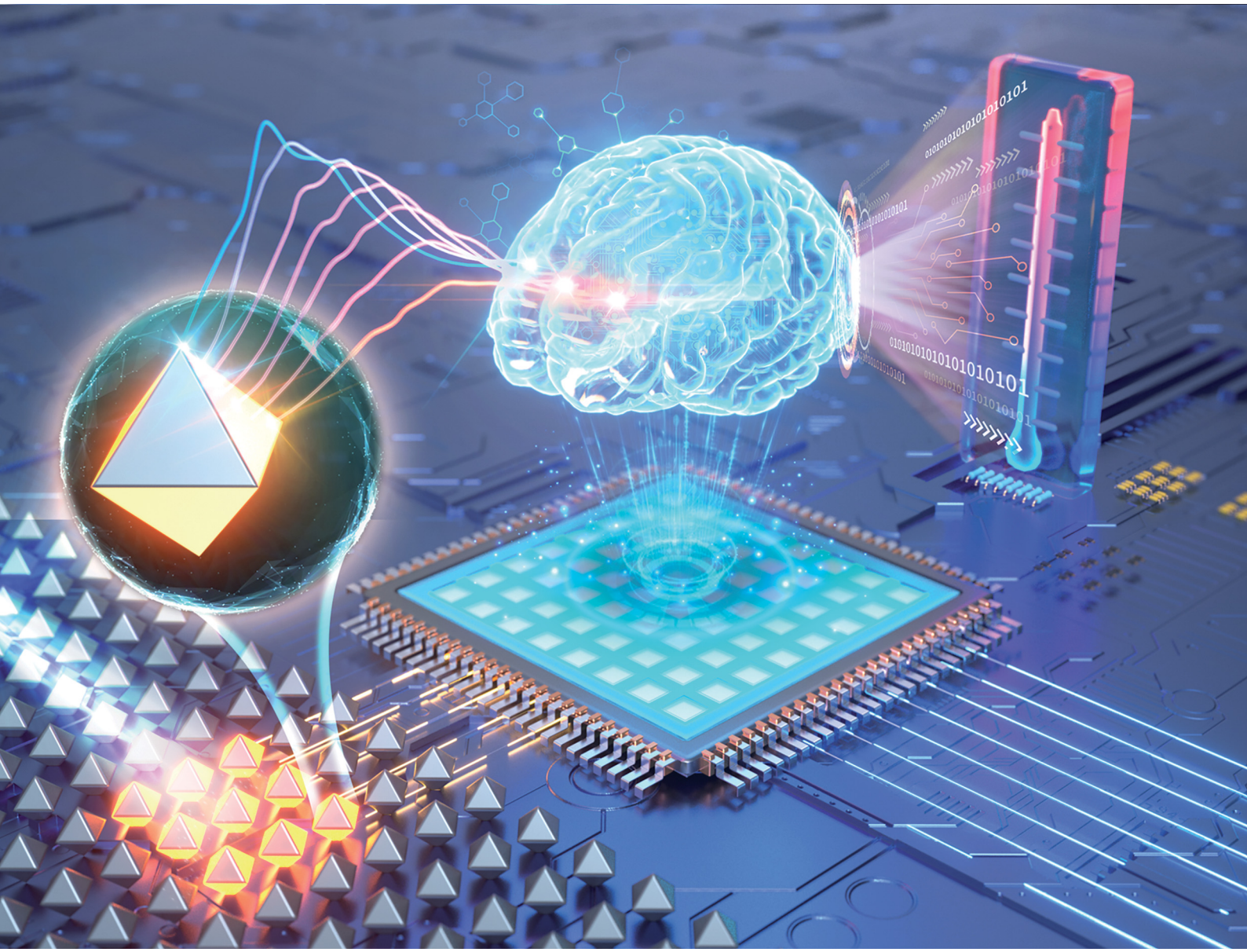

ISSN 2050-7526

ROYAL SOCIETY OF CHEMISTRY

PAPER

Maohui Yuan, Kai Han *et al.*

Achieving high-accuracy multi-feature temperature sensing in chromium(III)-doped nanophosphors using machine learning

Journal of Materials Chemistry C

ROYAL SOCIETY OF CHEMISTRY

PAPER

View Article Online
View Journal | View Issue

Cite this: J. Mater. Chem. C, 2025, 13, 18649

Achieving high-accuracy multi-feature temperature sensing in chromium(III)-doped nanophosphors using machine learning

Yijie Wen,†[abc] Xiang Feng,†[d] Chao Lin,[abc] Qianfan Zhang,[d] Maohui Yuan *[abc] and Kai Han *[abc]

Cr^{3+}-doped near-infrared luminescence thermometers, recognized for their tunable emission spectra and high temperature sensitivity, are extensively researched. Nonetheless, investigations into their temperature measurement capabilities have predominantly concentrated on ranges either below or above ambient temperature, with limited examination of broad-range measurements. Moreover, temperature assessments based on single spectral features are subject to uncertainties, whereas the integration of multiple features can enhance the temperature sensing accuracy. In this work, $K_2NaGaF_6:Cr^{3+}$ nanophosphors were synthesized *via* a hydrothermal method and their near-infrared luminescence was significantly enhanced through high-temperature annealing. Emission spectra were evaluated across a temperature span of 83 K to 573 K, and multiple spectral features were extracted for temperature sensing. Employing the auto-sklearn machine learning (ML) techniques, three spectral features—full width at half maximum (FWHM), peak intensity ratio, and integral area—were combined for temperature prediction. The optimized three-feature model achieved a temperature measurement root mean squared error (RMSE) of 0.52 K within the 223–323 K range, surpassing the performance of single- and two-feature models. Furthermore, the model also maintained an accuracy of RMSE $<$ 1 K over a wider measured temperature range. Our work demonstrates the superior high-accuracy temperature sensing based on the multiple features, and it can be used to measure the temperature in micro(nano)-scale applications.

Received 28th May 2025,
Accepted 3rd August 2025

DOI: 10.1039/d5tc02094h

rsc.li/materials-c

Introduction

Temperature is one of the seven fundamental physical quantities, and its effective measurement is critically important. Traditional contact-based temperature measurement techniques are often inadequate for challenging environments, such as those involving irregularly shaped surfaces, corrosive or radioactive conditions, enclosed transparent spaces, and areas with strong electric or magnetic fields. Non-contact optical temperature measurement technology, utilizing luminescence temperature-sensing materials can circumvent these limitations. As a non-contact temperature sensing approach, luminescent temperature detection provides the advantage of operating in micro-scale environments and maintaining efficiency under complex conditions.[1] Consequently, there has been growing interest within the scientific community in recent years regarding the research of non-contact optical temperature measurement methods and their applications across various technical domains.[2–11]

Different micro-nano materials have been used for temperature measurement, with rare earth ions (RE^{3+}) and transition metal ions being commonly employed for doping. RE^{3+} primarily rely on 4f–4f electron transitions, which are shielded by outer orbitals, making the excitation and emission of RE^{3+} doped fluorescent materials largely unaffected by the matrix structure and crystal field.[12] As a result, these materials exhibit sharp spectral peaks but poor tuning performance. In contrast, phosphors doped with a transition metal ion, such as Cr^{3+}, are highly sensitive to their position in the crystal field due to their unique $3d^3$ electronic structure. This allows its emission properties to be significantly adjusted by the crystal field, resulting in excellent tunability. When Cr^{3+} is doped into the low phonon

[a] College of Advanced Interdisciplinary Studies, National University of Defense Technology, Changsha, 410073, China. E-mail: yuanmaohui17@nudt.edu.cn, hankai0071@nudt.edu.cn
[b] Nanhu Laser Laboratory, National University of Defense Technology, Changsha, 410073, China
[c] Hunan Provincial Key Laboratory of High Energy Laser Technology, National University of Defense Technology, Changsha, 410073, China
[d] School of Materials Science and Engineering, Beihang University, Beijing, 100191, China
† The author contributed equally to the first author in this study.

energy fluoride hosts,[13] it can reduce thermal quenching and enable a broad-range temperature measurement. Additionally, Cr^{3+} can be excited by the cost-effective blue LEDs and emit light in the near-infrared band.[14,15] This large Stokes shift minimizes interference between the fluorescence signal and the excitation light.

In recent years, Cr^{3+} doped near-infrared phosphors have gained attention for optical temperature measurements, due to their high sensitivity, especially below 400 K.[16–19] However, their sensitivity diminishes above 400 K.[20–23] Moreover, previous research studies predominantly target temperature ranges either below or above room temperature, with limited studies addressing a comprehensive range that includes both extremes.[24,25] Typically, temperature analysis relies on a single feature, such as FWHM, fluorescence intensity, lifetime, *etc.*,[9,26,27] which would lead to the uncertainties for temperature sensing. Utilizing multiple features for temperature prediction can reduce uncertainties and enhance accuracy, yet few studies have pursued this approach.[28] Therefore, developing fluorescent temperature probes that operate across a broad temperature range and leverage multi-feature analysis could significantly improve measurement accuracy and expand application possibilities. Currently, ML has been the primary focus of attention and applied in various sensing applications, including gas and liquid concentration detection,[29–31] pressure sensing,[32] spectral material classification,[33] food analysis,[34–37] biology sensing,[38,39] flexible sensing,[40,41] temperature sensing[42–45] and other fields. Nevertheless, few attempts have been made to apply ML for temperature measurement based on fluorescence spectroscopy. Especially, the multiple features of the luminescence spectrum, such as intensity, FWHM, and peak intensity ratio, are well suited for predicting the temperature using the ML to improve the accuracy of temperature sensitivity.

Since fluorides exhibit low phonon energy, reduced thermal quenching, and a broad operating temperature range, K_2NaGaF_6:Cr^{3+} nanophosphors were synthesized using a green and environmentally friendly hydrothermal method (Part 1 in the SI).[15] It exhibits high stability at high temperatures, which provides a favorable stable condition to conduct accurate temperature measurements over a wide temperature range. Notably, under the excitation of a 450 nm laser, the luminescence characteristics and thermometric performance of these nanophosphors can be enhanced through the high-temperature annealing process. We analysed the morphology, structure, and luminescence of the nanophosphors before and after annealing, examining their emission spectra from 83 K to 573 K. Using ML, we combined three features—FWHM, peak intensity ratio, and integral area of the luminescence spectra to predict temperature. The auto-sklearn[46] technique was used for model training and hyperparameter tuning. The resulting multi-feature model exhibited a low RMSE of only 0.52 K over the temperature range of 223–323 K. Moreover, despite the limited data available, the RMSE maintained less than 1 K at lower temperature (118–128 K) and higher temperature (418–428 K) ranges. A comparative analysis between multi-feature and single-feature models revealed that model accuracy improved with the increase of feature numbers. In summary, by utilizing the multi-feature ML methodology based on K_2NaGaF_6:Cr^{3+} phosphor materials, we successfully achieved robust temperature measurements across a wide temperature range, underscoring the efficacy of the multi-feature combined ML model for temperature prediction based on sample fluorescence spectra.

Results and discussion

Fig. 1a shows the emission spectra of K_2NaGaF_6 doped with different Cr^{3+} concentrations under the excitation of 450 nm. There is an obvious broad peak centered at 740 nm, which is originated from the transition of $^4T_2 \rightarrow {}^4A_2$ of Cr^{3+}. The luminescence intensity initially increases and subsequently decreases with rising the doping concentration, with the optimal concentration identified at approximately 7 mol% (Fig. 1b). Notably, the peak position of the spectrum remains unchanged with increasing doping concentration (Fig. 1c). This phenomenon can be attributed to the similarity in ionic radii between Cr^{3+} (R = 0.615 Å, CN = 6) and Ga^{3+} (R = 0.620 Å, CN = 6), allowing Cr^{3+} to be effectively incorporated into the octahedral lattice sites, with minimal impact on the crystal volume.

Notably, the luminescence intensity of these fabricated nanophosphors can be significantly enhanced after annealing

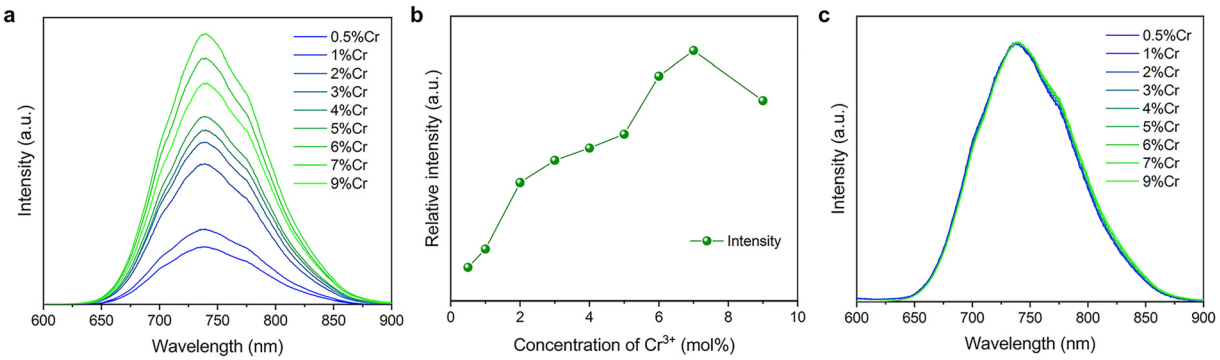

Fig. 1 (a) PL spectra, (b) peak intensity, and (c) normalized emission spectra of K_2NaGaF_6 nanophosphors doped with different Cr^{3+} concentrations.

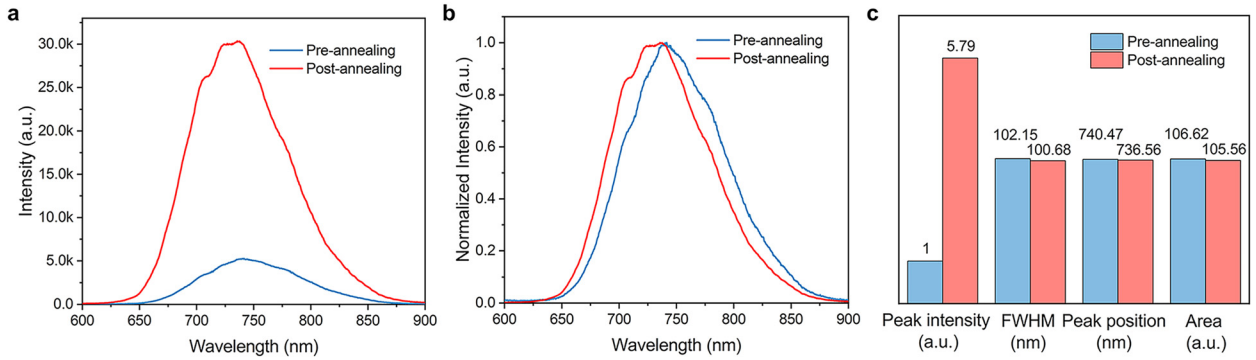

Fig. 2 (a) PL spectrum, (b) normalized PL spectrum, and (c) maximum peak intensity, FWHM, maximum peak position, and integral area of the K_2NaGaF_6:6 mol% Cr^{3+} nanophosphors pre- and post-annealing at 873 K temperature.

at 873 K, as shown in Fig. 2a. The luminescence intensity for the K_2NaGaF_6:6 mol% Cr^{3+} was enhanced approximately 6 times compared to the as prepared nanophosphors. Furthermore, the luminescence spectrum's profile underwent alterations post-annealing, as depicted in Fig. 2b. Specifically, the emission peak exhibited a blue shift, and two additional distinct smaller peaks emerged on the left side of the primary peak. In this context, K_2NaGaF_6:6 mol% Cr^{3+} was utilized as a representative example, although similar phenomena were observed across other concentrations, which displayed variations in peak shape and fluorescence enhancement ratio pre- and post-annealing. Detailed procedural steps are provided in Part 2 of the SI. After post-annealing, the photoluminescence (PL) spectral intensity was notably enhanced, the FWHM was marginally reduced, and the position of the maximum peak experienced a blue shift, as illustrated in Fig. 2c. These findings suggest that the annealing process significantly alters the fluorescence characteristics of the nanophosphors.

To further investigate the impact of the annealing process on the morphology and crystalline structure of the samples, we conducted scanning electron microscope (SEM) and X-ray diffraction (XRD) analyses on samples with varying doping concentrations, both pre- and post-annealing. A comparison of the SEM and XRD patterns before and after annealing (Fig. 3)

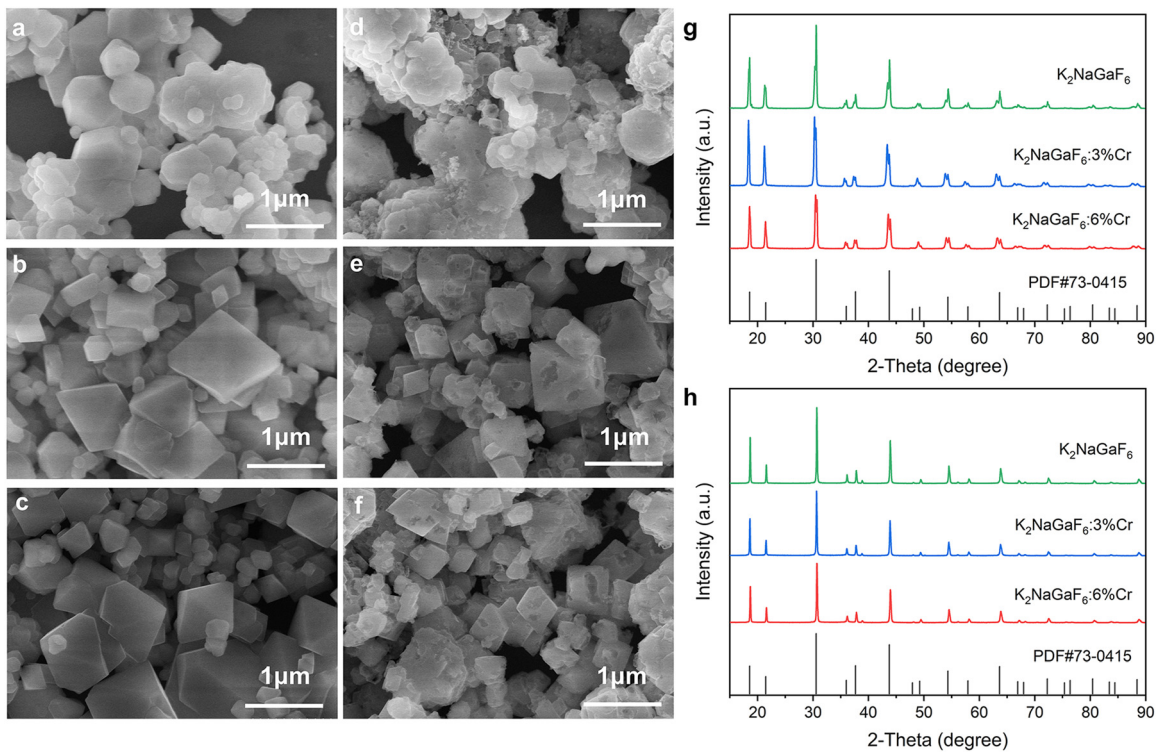

Fig. 3 SEM images of K_2NaGaF_6:Cr^{3+} nanophosphors doped with (a) 0 mol% (b) 3 mol% (c) 6 mol% Cr^{3+} concentrations before annealing. SEM images of K_2NaGaF_6:Cr^{3+} nanophosphors doped with (d) 0 mol% (e) 3 mol% (f) 6 mol% Cr^{3+} after annealing. XRD patterns of K_2NaGaF_6:Cr^{3+} nanophosphors doped with different Cr^{3+} concentrations (g) before annealing and (h) after annealing.

reveals that annealing significantly influences the morphology of the samples. It is hypothesized that high temperatures eliminate impurities, such as residual organic molecules on the sample surfaces, thereby mitigating their impact on fluorescence emission. Additionally, post-annealing XRD peaks exhibit reduced width and fewer extraneous peaks, aligning more closely with standard reference patterns. Furthermore, there is a slight shift of the high-angle peak towards a larger angle compared to pre-annealing observations. These findings further substantiate that high-temperature annealing enhances the crystalline density of the sample and improves its quantum efficiency. We conducted measurements of the photoluminescence excitation (PLE) and PL spectra of the sample both before and after annealing, as depicted in Fig. S4. It was observed that the peak wavelength of the PL spectrum exhibited a shift towards shorter wavelength after post-annealing. Similarly, the $^4A_2 \rightarrow {}^4T_2(F)$ peak position in the PLE spectrum also demonstrated a shift towards shorter wavelengths to a certain extent. Calculations performed using eqn (S1)–(S3) suggest that the crystal field strength increases following high temperature annealing.[47] This enhancement in the crystal field is likely attributed to a reduction in the crystal plane distance and a decrease in unit cell volume inducted by annealing, as detailed in Part 3 of the SI. Furthermore, the observed trend in the temperature-dependent behavior of annealed nanophosphors (Fig. S5) aligns with the findings of Jia *et al.*[48] The broadband emission peak ranging from 675 nm to 850 nm is attributed to the $^4T_2 \rightarrow {}^4A_2$ transition, with a calculated Huang–Rhys parameter of approximately 3.3, as elaborated in Part 4 of the SI. The electron–phonon coupling (EPC) effect contributes to the broadband emission and significant Stokes shift of the $^4T_2(F) \rightarrow {}^4A_2$ transition, as well as an increased FWHM at elevated temperatures, with the FWHM expanding from 79 nm at 83 K to 124 nm at 573 K. In Fig. S5, the PL spectra at varying temperatures exhibit irregularities, characterized by numerous minor peak fluctuations adjacent to the zero-phonon line (ZPL), which we attribute to phonon sidebands. As the temperature increases, the phonon sidebands on the lower energy side of the ZPL progressively diminish, whereas those on the higher energy side intensify, accompanied by a blue shift phenomenon.[49]

The nanophosphor, which demonstrates enhanced luminescence performance post-annealing, was utilized in a variable temperature experiment. At a temperature of 723 K, the fluorescence intensity is nearly extinguished. Consequently, to maintain a high signal-to-noise ratio, we selected a temperature range of 83 K to 573 K for optical temperature measurements. Within this range, notable changes in the intensity and shape of the PL spectrum are observed (c). Fig. 4d further displays the normalized spectra at different temperatures. It can be seen that the shape of the fluorescence spectrum changes obviously

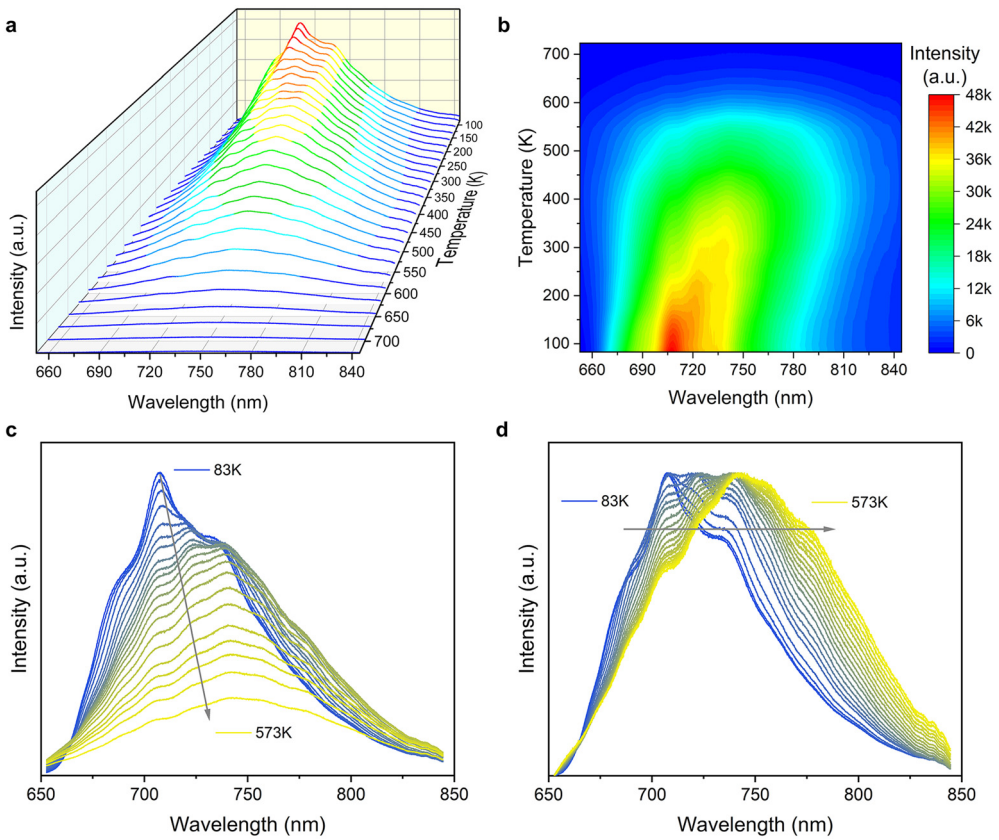

Fig. 4 (a) PL spectra and (b) PL mapping of $K_2NaGaF_6:Cr^{3+}$ nanophosphors as a function of temperature range of 83–723 K. (c) Original and (d) normalized PL spectra of K_2NaGaF_6:6 mol% Cr^{3+} nanophosphors under the different temperatures.

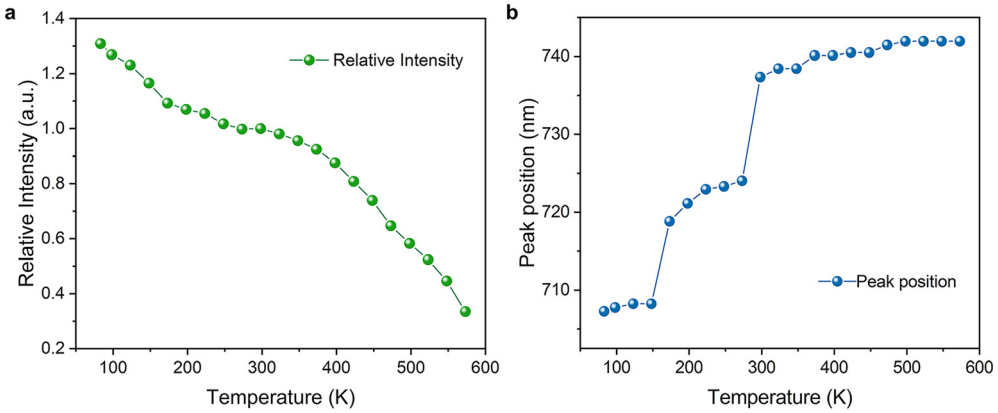

Fig. 5 (a) Relative intensity and (b) maximum peak position of the $K_2NaGaF_6:Cr^{3+}$ nanophosphors as a function of temperature.

with the increase of temperature, which is mainly manifested as the change of the relative intensity of the three peaks (708, 722 and 740 nm). The left 708 nm peak is largest at low temperature, the middle 722 nm peak is the highest at about 248 K, and the right 740 nm peak is the highest at high temperature (Fig. 5b). When the temperature exceeds 298 K, both the three peaks decrease as the temperature gradually increases.

Fig. 5a illustrates the correlation between the relative intensity of the spectra and temperature using the relative intensity at 298 K as a reference point (set to 1). Analysing the maximum peak position in Fig. 5b in relation to temperature variations reveals that the attenuation rate of peaks at shorter wavelengths is more pronounced. We hypothesize that the strong coupling between the shorter wavelength position and the ZPL results in a more significant EPC effect, thereby making the intensity at this position highly sensitive to temperature changes. Fig. 5b depicts the maximum peak position of the spectrum across different temperatures. As temperature rises, the position of the maximum peak continuously shifts upward. This phenomenon can be attributed to the thermal expansion of the crystal lattice, which reduces the crystal field strength, consequently altering the energy level positions and causing a red shift in the peak (Part 5 of the SI). Additionally, the peak intensity ratio at 740 nm and 708 nm, FWHM and integrated area values of the normalized spectrum at various temperatures were extracted and plotted against temperature, as shown in Fig. 6. Using the polynomial fitting operation, the well-fitted results obtained indicate the monotonous trend of the three spectral features with respect to temperature. Especially, the FWHM and the integral integrated area have a clear physical meaning, and obey the Boltzmann distribution law (see Part 7 of the SI). In addition, we further verified the stability of the spectra under the high temperatures (see Part 8 of the SI), and the spectral data demonstrate high stability and repeatability at high temperatures. These results further prove that it is suited for temperature detection and prediction.

Temperatures were selected ranging from 223 K to 323 K with intervals of 0.5 K, resulting in a total of 201 temperature points. At each temperature, we conducted 10 measurements, yielding a total of 2010 spectra signals. Each spectrum was processed to extract three features: FWHM, the ratio of $I_{740\,nm}/I_{708\,nm}$ (ratio), and the integral area (area). As shown in Fig. 6, all three features vary monotonically with temperature and exhibit high sensitivity to temperature changes, making them well-suited for temperature prediction. In summary, our ML dataset includes 2010 samples, each consisted of three features and a temperature label. The dataset was split into a training set and a test set in a 3 : 1 ratio. To enhance data utilization, no additional validation set was created. Instead, five-fold cross-validation was employed, allowing the training set to simultaneously support model training and

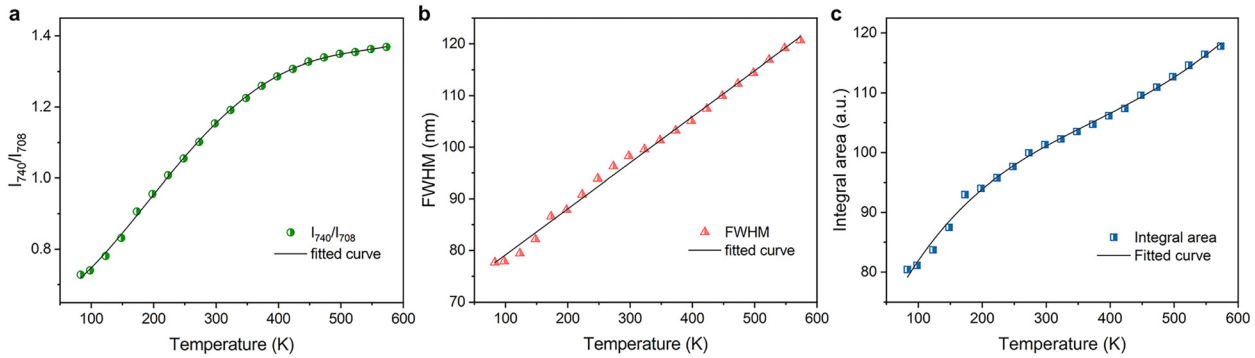

Fig. 6 (a) Peak intensity ratio, (b) FWHM, and (c) integral area of $K_2NaGaF_6:Cr^{3+}$ nanophosphors as functions of the temperature.

Table 1 Comparison of single-feature and three-feature model data of MAE, RMSE, MaxAE and R^2

Model	MAE (K)	RMSE (K)	MaxAE (K)	R^2
FWHM + ratio + area	0.4072	0.5208	2.3520	0.99968
FWHM + ratio	0.4219	0.5392	2.3530	0.99967
FWHM + area	0.4748	0.6094	2.1547	0.99956
Ratio + area	0.5731	0.7271	2.7237	0.99938
FWHM	0.4780	0.6096	2.0868	0.99956
Ratio	0.6512	0.8362	3.3809	0.99917
Area	1.2012	1.5455	6.4850	0.99718

hyperparameter tuning. The test set was used exclusively once to evaluate the performance of the optimized model, ensuring no data leakage and providing an accurate assessment of our model's true performance. The auto-sklearn method was introduced for the ML process. This method integrates three state-of-the-art ML techniques: meta-learning, Bayesian optimization and ensemble construction, enabling the automatic identification of the best-performing model from 12 algorithms [adaboost, ARD regression, decision tree, extra trees, Gaussian process, gradient boosting, *K*-nearest neighbors, support vector regression (LibLinear), support vector regression (LibSVM), multi-layer perceptron, random forest, and stochastic gradient descent]. Meta-learning leverages prior experience to provide reasonable initial model guesses based on the characteristics of the dataset. Starting from these initial guesses, the Bayesian optimization algorithm efficiently searches for the hyperparameter space to identify the best-performing model. Finally, auto-sklearn uses a greedy algorithm to construct an ensemble from the top 50 ranked models, combining their strengths to further enhance the robustness. To demonstrate the superiority of our multi-feature approach, we trained seven models using different combinations of features: FWHM + ratio + area, FWHM + ratio, FWHM + area, ratio + area, only FWHM, only ratio, and only area. Each model was trained using the auto-sklearn technique on a 20-core server for 1800 seconds. The performance of each model was evaluated using four metrics: mean absolute error (MAE), root mean squared error (RMSE), maximum absolute error (MaxAE), and the coefficient of determination (R^2) (Fig. S7 and Table 1).

Except for the MaxAE metric, the other three metrics for two-feature models consistently outperform those of the corresponding single-feature models. Similarly, the three-feature model outperforms all two-feature and single-feature models, clearly demonstrating the advantage of our multi-feature approach. The slight deviation of MaxAE from this trend can be attributed to the greater focus applied on individual samples rather than the overall statistics. The details of the auto-sklearn training process are described and summarized in Tables S1 and S2 in the SI.

Fig. 7(a–c) display the schematic diagram of a Cr^{3+}-doped nanophosphor thermometer using the multi-feature of the spectral data based on the auto-sklearn ML process. Fig. 7d shows the relationship between actual and predicted temperature values based on our ML model. The results indicate that the three-feature temperature prediction model shows higher accuracy than the single-feature or two-feature temperature

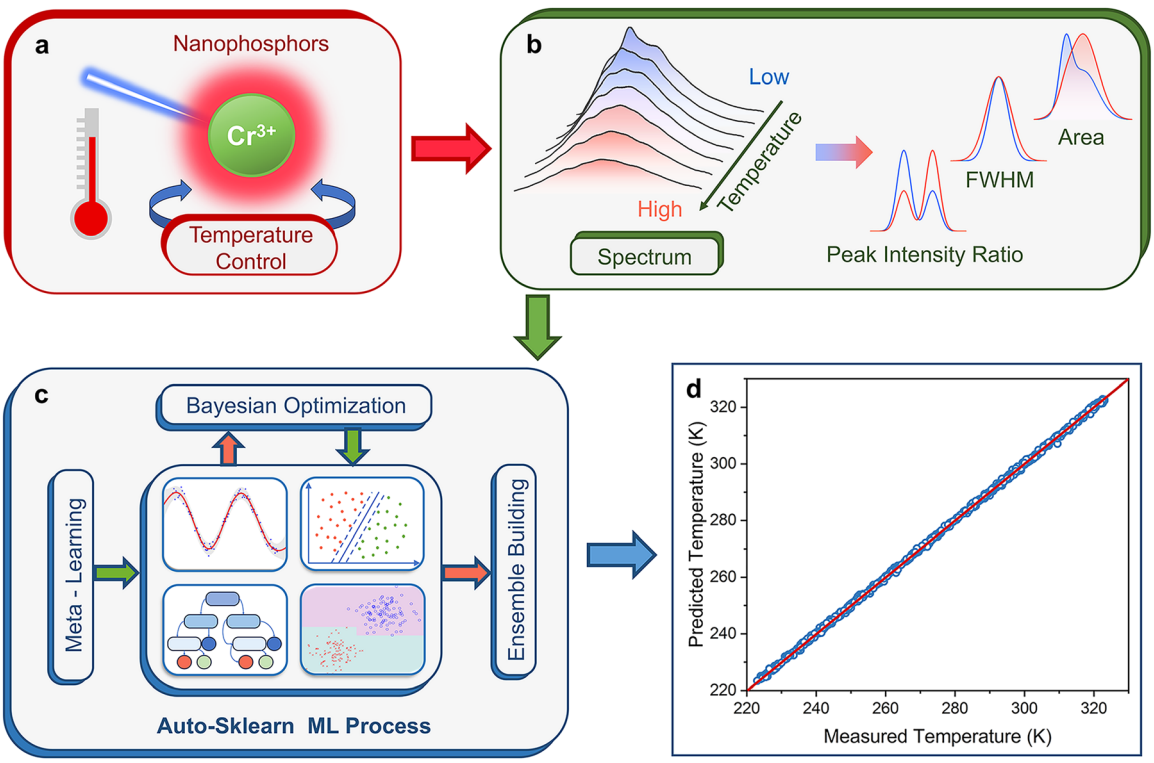

Fig. 7 (a) Schematic diagram of Cr^{3+}-doped nanophosphors thermometer. (b) The multi-feature of the spectral data for ML process. (c) The auto-sklearn ML process. (d) Predicted *vs.* measured temperature using the ML model.

prediction model. Previous studies have utilized the temperature sensitivity and uncertainty to evaluate the performance of a luminescent thermometer.[9,20,23,24] Notably, the single spectral feature for temperature measurement would be easily affected by the external environment. Here, the combination of multiple spectral features and multiple ML models can effectively avoid this problem. The temperature prediction accuracy after combining the three features can reach 0.52 K (RMSE), MAE ~0.4 K. Furthermore, we selected the 123 K, 248 K and 423 K as the three characteristic temperatures, trained and tested the spectral data. Compared with the spectral data operated at the range of 223–323 K, the temperature measurement accuracy of MAE ~0.7 K and RMSE less than 1 K can be achieved when the acquisition step is reduced by half and the temperature measurement accuracy is improved (Fig. S8 and Table S3). The results indicate that these nanophosphor thermometer based on the ML model can achieve high-precision temperature prediction in a relatively wide temperature range. This is a quite significant and competitive prediction deviation for temperature sensing based on our advanced model (Table S4). Our attempt proves that combining multiple features can indeed improve the accuracy of the temperature prediction, showcasing its potential for high-precision multi-feature temperature measurement in the micro/nano-scale applications.

Conclusions

In conclusion, we have successfully synthesized $K_2NaGaF_6:Cr^{3+}$ nanophosphors and observed the intensive near-infrared emission upon excitation at 450 nm. Annealing of the nanophosphors at 873 K significantly enhances the fluorescence emission intensity and modifies the spectral peak profile. The emission peak undergoes a blue shift, and two additional distinct peaks emerge alongside the original single peak. We hypothesize that high-temperature annealing removes surface impurities, such as organic residues, which adversely affect luminescence. Furthermore, annealing facilitates a more compact crystal structure, enhancing the crystal field strength and thereby increasing spectral emission intensity and altering peak profiles. Additionally, we observed that the relative intensities of these three peaks post-annealing exhibit a strong temperature dependence, offering a novel temperature-sensitive parameter for detection applications. We extracted three spectral features—peak intensity ratio, FWHM, and integral area—from the normalized spectra at various temperatures. These features were integrated using ML techniques for temperature detection. The predictive performance of the model utilizing a three-feature combination surpasses that of models employing single features. The nanophosphor facilitates temperature detection over an extensive range from 83 K to 573 K. Specifically, within the narrower range of 223 K to 323 K, the model attains a prediction accuracy of RMSE ~0.52 K. Moreover, the model maintains commendable sensing accuracy across a broader temperature spectrum. These findings underscore the viability of the nanophosphor for temperature detection and emphasize the enhanced accuracy achieved through ML, thereby augmenting its potential for practical applications.

Author contributions

Yijie Wen: methodology, investigation, visualization, data curation, writing – original draft. Xiang Feng: software, methodology, data curation. Chao Lin: software, investigation. Qianfan Zhang: data curation. Maohui Yuan: conceptualization, investigation, supervision, writing – review & editing. Kai Han: supervision, project administration, writing – review & editing.

Conflicts of interest

There are no conflicts to declare.

Data availability

The data supporting this article have been included as part of the SI. All other data in this study will be made available upon request from the corresponding author.

Supplementary information available: S1, Crystal structure; S2, Temperature-dependent PL spectra; S3, Additional PL spectra under before- and after-annealing; S4, PLE and PL spectra; S5, Normalized PL spectra; S6, Bond length results; S7, Metrics for ML models; S8, Predicted vs measured temperature results; S9, Relationship between FWHM and temperature; S10, Verification of the high-temperature stability; S11, Spectral data of the repetition. See DOI: **https://doi.org/10.1039/d5tc02094h**

Acknowledgements

This work was supported by the Huxiang Youth Talent Support Program (grant number 2021RC3074).

References

1 M. T. Abbas, N. Z. Khan, J. Mao, L. Qiu, X. Wei, Y. Chen and S. A. Khan, *Mater. Today Chem.*, 2022, **24**, 100903.
2 B. del Rosal, E. Ximendes, U. Rocha and D. Jaque, *Adv. Opt. Mater.*, 2017, **5**, 1600508.
3 B. Harrington, Z. Ye, L. Signor and A. D. Pickel, *ACS Nanosci. Au*, 2024, **4**, 30–61.
4 I. K. van Ravenhorst, R. G. Geitenbeek, M. J. van der Eerden, J. T. van Omme, H. H. P. Garza, F. Meirer, A. Meijerink and B. M. Weckhuysen, *ChemCatChem*, 2019, **11**, 5505–5512.
5 M. Back, J. Ueda, J. Xu, D. Murata, M. G. Brik and S. Tanabe, *ACS Appl. Mater. Interfaces*, 2019, **11**, 38937–38945.
6 R. G. Geitenbeek, J. C. Vollenbroek, H. M. H. Weijgertze, C. B. M. Tregouet, A.-E. Nieuwelink, C. L. Kennedy, B. M. Weckhuysen, D. Lohse, A. van Blaaderen, A. van den Berg, M. Odijk and A. Meijerink, *Lab Chip*, 2019, **19**, 1236–1246.

7 N. Yang, Z. Li, T. Zhou, Z. Zhang, W. Shi, Y. Tong and J. Shi, *J. Adv. Ceram.*, 2024, **13**, 821–833.
8 Y. Ma, A. Aierken, Y. Wang and A. Meijerink, *J. Colloid Interface Sci.*, 2023, **638**, 640–649.
9 M. Back, J. Ueda, M. G. Brik and S. Tanabe, *ACS Appl. Mater. Interfaces*, 2020, **12**, 38325–38332.
10 K. Li, Z. Huang and D. Zhu, *Ceram. Int.*, 2025, **51**, 17433–17444.
11 Z. Huang, K. Li, Z. Zhang, J. Liu and D. Zhu, *J. Mater. Chem. C*, 2025, **13**, 4564–4575.
12 M. Jia, X. Chen, R. Sun, D. Wu, X. Li, Z. Shi, G. Chen and C. Shan, *Nano Res.*, 2023, **16**, 2949–2967.
13 F. Zhao, Z. Song and Q. Liu, *Laser Photonics Rev.*, 2022, **16**, 2200380.
14 G. Liu, W. Chen, Z. Xiong, Y. Wang, S. Zhang and Z. Xia, *Nat. Photonics*, 2024, **18**, 562–568.
15 H. Yu, J. Yang, Y. Liu, C. Xie, Z. Huang and L. Mei, *ACS Sustainable Chem. Eng.*, 2022, **10**, 8022–8030.
16 D. Chen, S. Liu, Y. Zhou, Z. Wan, P. Huang and Z. Ji, *J. Mater. Chem. C*, 2016, **4**, 9044–9051.
17 K. Maciejewska and L. Marciniak, *Chem. Eng. J.*, 2020, **402**, 126197.
18 L. Marciniak and A. Bednarkiewicz, *Sens. Actuators, B*, 2017, **243**, 388–393.
19 K. Elzbieciak-Piecka, M. Suta and L. Marciniak, *Chem. Eng. J.*, 2021, **421**, 129757.
20 M. Back, E. Trave, J. Ueda and S. Tanabe, *Chem. Mater.*, 2016, **28**, 8347–8356.
21 L. Zhou, Z. Lyu, D. Sun, S. Shen, T. Tan, L. Wang, H. Zhao and H. You, *Adv. Opt. Mater.*, 2022, **10**, 2201308.
22 A. L. Mullins, A. Ćirić, I. Zeković, J. A. G. Williams, M. D. Dramićanin and I. R. Evans, *J. Mater. Chem. C*, 2022, **10**, 10396–10403.
23 M. Han, S. Chen, J. Li, Z. Gao, Y. Zhang, Y. Shen, Y. Tian and D. Deng, *J. Alloys Compd.*, 2024, **973**, 172927.
24 J. Ou, S. Fang, Q. Zhu, Y. Zhai, H. Zhang and L. Wang, *Phys. Chem. Chem. Phys.*, 2023, **25**, 16866–16871.
25 Q. Zhang, G. Li, G. Li, D. Liu, P. Dang, L. Qiu, H. Lian, M. S. Molokeev and J. Lin, *Adv. Opt. Mater.*, 2024, **12**, 2301429.
26 D. Chen, Z. Wan, Y. Zhou and Z. Ji, *J. Eur. Ceram. Soc.*, 2015, **35**, 4211–4216.
27 R. Li, G. Wei, Z. Wang, Y. Wang, J. Li, S. He, L. Li, H. Suo, W. Ding and P. Li, *Laser Photonics Rev.*, 2023, **17**, 2200589.
28 D. Sevic, M. S. Rabasovic, J. Krizan, S. Savic-Sevic, M. G. Nikolic, B. P. Marinkovic and M. D. Rabasovic, *J. Phys. D: Appl. Phys.*, 2019, **53**, 015106.
29 A. Döring and A. L. Rogach, *ACS Appl. Nano Mater.*, 2022, **5**, 11208–11218.
30 H. Li, H. Yue, H. Li, M. Zhu, X. He, M. Liu, X. Li and F. Qiu, *J. Colloid Interface Sci.*, 2025, **680**, 389–404.
31 Z. Yang, S. Lv, Y. Zhang, J. Wang, L. Jiang, X. Jia, C. Wang, X. Yan, P. Sun, Y. Duan, F. Liu and G. Lu, *Nano-Micro Lett.*, 2022, **14**, 56.
32 H. J. Lee, J. C. Yang, J. Choi, J. Kim, G. S. Lee, S. P. Sasikala, G.-H. Lee, S.-H. K. Park, H. M. Lee, J. Y. Sim, S. Park and S. O. Kim, *ACS Nano*, 2021, **15**, 10347–10356.
33 M. Chatzidakis and G. A. Botton, *Sci. Rep.*, 2019, **9**, 2126.
34 S. Weng, H. Yuan, X. Zhang, P. Li, L. Zheng, J. Zhao and L. Huang, *Analyst*, 2020, **145**, 4827–4835.
35 B. C. Geronimo, S. M. Mastelini, R. H. Carvalho, S. B. Júnior, D. F. Barbin, M. Shimokomaki and E. I. Ida, *Infrared Phys. Technol.*, 2019, **96**, 303–310.
36 S. B. Junior, S. M. Mastelini, A. P. A. C. Barbon, D. F. Barbin, R. Calvini, J. F. Lopes and A. Ulrici, *Infrared Phys. Technol.*, 2020, **7**, 342–354.
37 T. Dramićanin, I. Zeković, J. Periša and M. D. Dramićanin, *J. Fluoresc.*, 2019, **29**, 1103–1111.
38 S. Ye, K. Zhong, J. Zhang, W. Hu, J. D. Hirst, G. Zhang, S. Mukamel and J. Jiang, *J. Am. Chem. Soc.*, 2020, **142**, 19071–19077.
39 F. Lussier, D. Missirlis, J. P. Spatz and J.-F. Masson, *ACS Nano*, 2019, **13**, 1403–1411.
40 Y. Lu, D. Kong, G. Yang, R. Wang, G. Pang, H. Luo, H. Yang and K. Xu, *Adv. Sci.*, 2023, **10**, 2303949.
41 H. Liu, H. Xiang, Y. Wang, Z. Li, L. Qian, P. Li, Y. Ma, H. Zhou and W. Huang, *ACS Appl. Mater. Interfaces*, 2019, **11**, 40613–40619.
42 M. S. Rabasovic, S. Savic-Sevic, J. Križan, B. Matovic, M. Nikolic and D. Sevic, *Phys. Scr.*, 2023, **98**, 116003.
43 J. Z. Jelic, A. Dencevski, M. D. Rabasovic, J. Krizan, S. Savic-Sevic, M. G. Nikolic, M. H. Aguirre, D. Sevic and M. S. Rabasovic, *Photonics*, 2024, **11**, 642.
44 E. Ximendes, R. Marin, L. D. Carlos and D. Jaque, *Light: Sci. Appl.*, 2022, **11**, 237.
45 A. Döring, Y. Qiu and A. L. Rogach, *ACS Appl. Nano Mater.*, 2024, **7**, 2258–2269.
46 M. Feurer, A. Klein, K. Eggensperger, J. T. Springenberg, M. Blum and F. Hutter, *Proceedings of the 29th annual conference on neural information processing systems (NIPS)*, 2015, **28**, 2962–2970.
47 Z. Song, P. A. Tanner and Q. Liu, *J. Phys. Chem. Lett.*, 2024, **15**, 2319–2324.
48 Z. Jia, C. Yuan, Y. Liu, X. Wang, P. Sun, L. Wang, H. Jiang and J. Jiang, *Light: Sci. Appl.*, 2020, **9**, 86.
49 Z. Liao, Y. Li, J. Zuo, G. Chen, H. Liang, S. Wu, J. Peng and X. Ye, *Dalton Trans.*, 2023, **52**, 5587–5596.

